A Consistent Treatment of Microwave Emissivity and Radar Backscatter for Retrieval of Precipitation over Water Surfaces

S. Joseph Munchak*

Earth System Science Interdisciplinary Center, University of Maryland, College Park

Robert Meneghini

NASA Goddard Space Flight Center, Greenbelt, MD

Mircea Grecu

Morgan State University, Baltimore, MD

William S. Olson

Joint Center for Earth System Technology, University of Maryland Baltimore County, Baltimore, MD

**Corresponding author address:* Mesoscale Atmospheric Processes Laboratory, NASA Goddard Space Flight Center, 8800 Greenbelt Rd, Greenbelt, MD 20771.

E-mail: s.j.munchak@nasa.gov

ABSTRACT

The Global Precipitation Measurement satellite's Microwave Imager (GMI) and Dual-frequency Precipitation Radar (DPR) are designed to provide the most accurate instantaneous precipitation estimates currently available from space. The GPM Combined Algorithm (CORRA) plays a key role in this process by retrieving precipitation profiles that are consistent with GMI and DPR measurements; therefore it is desirable that the forward models in CORRA use the same geophysical input parameters. This study explores the feasibility of using internally consistent emissivity and surface backscatter cross section (σ_0) models for water surfaces in CORRA. An empirical model for DPR Ku and Ka σ_0 as a function of 10m wind speed and incidence angle is derived from GMI-only wind retrievals under clear conditions. This allows for the σ_0 measurements, which are also influenced by path-integrated attenuation (PIA) from precipitation, to be used as input to CORRA and for wind speed to be retrieved as output. Comparisons to buoy data give a wind rmse of 3.7 m/s for Ku+GMI and 3.2 m/s for Ku+Ka+GMI retrievals under precipitation (compared to 1.3 m/s for clear-sky GMI-only), and there is a reduction in bias from the GANAL background data (-10%) to the Ku+GMI (-3%) and Ku+Ka+GMI (-5%) retrievals. Ku+GMI retrievals of precipitation increase slightly in light (< 1 mm/hr) and decrease in moderate to heavy precipitation (> 1mm/hr). The Ku+Ka+GMI retrievals, being additionally constrained by the Ka reflectivity, increase only slightly in moderate and heavy precipitation at low wind speeds (< 5 m/s) relative to retrievals using the surface reference estimate of PIA as input.

1. Introduction

Algorithms for estimating precipitation from space-borne radars at attenuating frequencies (e.g., TRMM PR (Iguchi et al. 2000, 2009), CloudSat (Mitrescu et al. 2010), GPM DPR (Grecu et al. 2011)) have long realized the benefit of an estimate of the path-integrated attenuation (PIA) that is independent of the reflectivity profile for the purposes of constraining the integrated and surface precipitation amount. In general, such an estimate of the PIA is obtained via a form of the surface reference technique (SRT; (Meneghini et al. 2000, 2004)), which subtracts the surface radar backscatter cross-section (σ_0) in a precipitating column from a precipitation-free reference. The difference is then assumed to be due to attenuation from precipitation after accounting for multiple scattering (Battaglia and Simmer 2008) and the effect of precipitation on the surface itself (Seto and Iguchi 2007). If the ratio of this difference to the uncertainty in the reference value, known as the reliability factor, is large, then the precipitation retrieval is more strongly constrained, because the PIA is sensitive to the vertically-integrated third moment of the particle size distribution whereas the reflectivity is sensitive to the sixth moment.

Algorithms that make simultaneous use of passive microwave and radar data (Haddad et al. 1997; Grecu et al. 2004; Munchak and Kummerow 2011) generally use the SRT PIA along with microwave radiances to constrain the precipitation profile (indeed, PIA can be the dominant constraint because of its high resolution relative to the passive microwave footprint, especially when the reliability factor is large). These algorithms also require knowledge of the surface emissivity in order to forward model the brightness temperatures for comparison to observations. Since emission and reflection are related processes, it is logical for a combined algorithm to exploit any relationships between σ_0 and emissivity that may exist. Over water surfaces, it is known that wind-induced surface roughness and foam have a large impact on σ_0 and emissivity; thus, it should benefit a combined algorithm to retrieve the 10m wind speed in order to achieve internal consistency between the forward-modeled PIA and brightness temperatures.

The purpose of this work is not only to highlight the benefits of unifying the active and passive surface characteristics for the purpose of precipitation retrievals from GPM, but also to demonstrate the feasibility of combined DPR-GMI retrievals of surface wind over water, particularly when precipitation is present. This has historically been problematic for both passive and active (scatterometer) wind retrievals (Weissman et al. 2012), despite the high motivation to develop capabilities to monitor the strength of tropical and extratropical cyclones. For passive measurements, higher frequency channels ($>$ 19 GHz) can become opaque to the surface in rain and clouds, and although the surface emission is not fully obscured at lower frequencies, measurements at multiple frequencies near the C-band are required to distinguish the surface and rain column contributions to the observed radiances (Uhlhorn et al. 2007). However, the large footprints that are characteristic of spaceborne microwave radiometers at these frequencies are not optimal for retrievals of wind and precipitation due to non-uniformity within the footprint. Even outside of rain, cross-talk between wind, water vapor and cloud liquid water can bias wind retrievals (O'Dell et al. (2008); Rapp et al. (2009)). Also, rain creates an additional source of surface waves, which can either enhance or damp surface backscatter, depending on angle, frequency, and wind speed (Stiles and Yueh (2002), Seto and Iguchi (2007)). Backscattering from the rain itself can also enhance the measured surface cross-section, particularly for scatterometers that are designed to maximize signal-to-noise ratio by employing relatively long pulse widths and large footprint sizes (Li et al. 2002). Finally, in high winds the sensitivity of σ_0 to wind speed is low (Donnelly et al. (1999); Fernandez et al. (2006)), limiting the accuracy of retrievals even if rain effects are accounted for.

As of yet, only the short-lived Midori-II AMSR-SeaWinds combination of passive and active instruments have been designed specifically for the measurement of ocean winds, but several investigators have taken advantage of existing platforms with these measurements (e.g., TRMM and Aquarius) or coincident overpasses of scatterometer and passive microwave radiometers to elucidate further information about the atmosphere and sea state than is possible from either instrument type alone. Studies based on the TRMM microwave imager (TMI) and precipitation radar (PR) have often used the TMI-based wind retrievals as a reference to develop geophysical model functions (GMFs) for PR, which relate wind speed and σ_0 (e.g., Li et al. (2002); Freilich and Vanhoff (2003); Tran et al. (2007)). These are then used to retrieve the wind field independently with PR (Li et al. 2004) either as a standalone product or for use as a reference to estimate the rain-induced attenuation as an input to the rainfall estimation algorithms. In the case of WindSat, a comparison of its retrievals and QuickScat wind vectors in coincident overpasses was performed by Quilfen et al. (2007), who found differences between the two depended on wind speed and water vapor (a consequence of the aforementioned cross-talk between parameters). The authors also attempted to combine the two sets of measurements via multiple regression. They found that adding QuickScat to WindSat did not improve wind retrievals outside of rain, but they did note a slight improvement under raining conditions. More recently, the Aquarius satellite, which offers active and passive measurements at L-band for the purpose of ocean salinity retrieval, was launched. Yueh et al. (2013) developed GMFs based on SSM/I and NCEP reanalysis colocations and found that the resulting combined active-passive retrievals of wind speed and salinity compared favorably to salinity retrievals where ancillary data was used to set the wind vector.

The growing number of satellites with active and passive microwave instruments (e.g., TRMM, GPM, Aquarius, SMAP), along with airborne platforms (e.g., the NASA Global Hawk Hurricane and Severe Storm Sentinel-HS3) represents an opportunity to use these combinations to retrieve ocean winds, particularly under conditions (such as rain) where single-sensor methods are underconstrained. This study is based on data from the Global Precipitation Measurement (GPM) satellite, which has a particularly useful set of measurements for developing the GMFs due to the well-calibrated, high resolution GPM Microwave Imager (GMI) instrument (Draper et al. 2015) and a dual-frequency precipitation radar (DPR) which improves the capability to separate surface effects from rain-induced attenuation. Our strategy (Figure 1) is to develop a GMF for DPR based upon co-located GMI wind retrievals, and then use this GMF under raining conditions by modifying the combined GPM DPR-GMI precipitation retrieval algorithm CORRA (Olson and Masunaga 2015). In order to have as accurate a wind reference as possible, we evaluate three emissivity models after calculating offsets under clear and calm conditions to achieve consistency with the GMI calibration. Next, we use all available matchups of GMI and DPR under non-precipitating conditions to develop the GMFs. This process is presented in section 2. Next, the use of GMFs in the GPM combined GMI-DPR ensemble filter retrieval framework, including validation of winds in regions of precipitation against buoy measurements, is described in section 3, followed by a summary in section 4.

2. Development of Geophysical Model Functions for DPR

Although physical models exist to describe the relationship between wind speed, the wave spectrum, and backscatter (Durden and Vesecky (1985); Majurec et al. (2014)), the desire for GPM applications is to be as internally consistent as possible between the emissivity model and DPR GMF. Therefore, the strategy in this study is to derive empirical GMFs from clear-sky matchups of DPR and GMI-derived 10m wind retrievals, eliminating as much as possible the error from precipitation and cloud cross-talk described in section 1, then apply those GMFs to retrievals under all conditions. The use of empirical GMFs derived in this manner is standard practice in the scatterometer community (Migliaccio and Reppucci 2006).

The first step in this process is to generate the clear-sky wind retrievals and then assess their error relative to buoy observations. In the absence of precipitation, the microwave radiances measured by GMI are primarily sensitive to the surface emission, atmospheric temperature and water vapor profile, and cloud liquid water. These parameters can be solved for using optimal estimation, also known as variational, retrieval techniques. These have been implemented for microwave sensors by Elsaesser and Kummerow (2008) and Boukabara et al. (2011), and a blend of their approaches is used to derive the surface and atmospheric properties from GMI by minimizing the cost function:

$$J = (\mathbf{x}-\mathbf{x_a})^T \mathbf{S_x}^{-1}(\mathbf{x}-\mathbf{x_a}) + (\mathbf{y}-f(\mathbf{x}))^T \mathbf{S_y}^{-1}(\mathbf{y}-f(\mathbf{x})). \quad (1)$$

The components of the optimal estimation retrieval are the state vector ($\mathbf{x}$) and covariance matrix ($\mathbf{S_x}$), the observation vector ($\mathbf{y}$) and covariance matrix ($\mathbf{S_y}$), and forward model $f(\mathbf{x})$. For water surfaces, the state vector consists of the 10m wind speed, cloud liquid water path, and a set of variables representing the values of the leading empirical orthogonal functions (EOFs) of the atmospheric temperature and water vapor profile. These EOFs were derived from 10 years of MERRA reanalysis (Rienecker et al. (2011); NASA/GMAO (2008)) independently in 1K SST bins. The number of leading EOFs is chosen such that at least 99% of the variance in temperature and water vapor is explained by the selected EOFs. The EOFS are used to simultaneously adjust the initial atmospheric temperature and water vapor profiles in order to match the observed GMI radiances. This is a change from the Elsaesser and Kummerow (2008) method, which assumed a constant lapse rate and scale height for water vapor. These assumptions are sufficient for matching observations near the 22-GHz water vapor absorption line, where radiances are mostly sensitive to the total column-integrated amount of water vapor and are less sensitive to its vertical structure and emitting temperature. However both the vertical structure of water vapor and temperature matter for modeling the additional channels near 183 GHz on GMI, so some method of adjusting the shape of the profile in mid and upper levels is necessary. The EOFs represent the climatological co-varying structures in temperature and water vapor profiles, and are a robust way to adjust both without requiring temperature sounding channels (e.g., 50-55 GHz). The *a priori* (and initial) state $\mathbf{x_a}$ is the MERRA reanalysis interpolated in time and space to the GMI pixel location.

Because the atmosphere is represented by EOFs and no covariance between the atmosphere and wind/cloud is assumed, the state covariance matrix $\mathbf{S_x}$ is diagonal. The observation vector consists of the 13-channel GMI radiances from the GMI Level 1C-R (intercalibrated and co-located) product (GPM Science Team 2015). The co-location matches the high-frequency (HF) observations (166V&H, 183±3, and 183±7 GHz), which are observed at 49.2° earth incidence angle, with the lower-frequency (LF) observations, which are observed at 52.8° earth incidence angle. A diagonal matrix for $\mathbf{S_y}$ is also assumed, with values of instrument noise (Hou et al. 2014) plus additional error determined from buoy matchups (Table 1) to account for forward model error and inexact footprint matching.

The forward model is derived from the Community Radiative Transfer Model (CRTM) Emission (non-scattering atmosphere) model, modified to include the downwelling path length correction for roughened water surfaces as described by Meissner and Wentz (2012) and using the same atmospheric layers that are provided by MERRA products up to 10 hPA. Absorption by atmospheric gases is calculated from Rosenkranz (1998) and Tretyakov et al. (2003). Cloud liquid absorption follows Liebe et al. (1991) and cloud water is assumed to follow an adiabatic profile (Albrecht et al. 1990). Since the surface emissivity and its relationship to wind speed is of fundamental importance to this study, three emissivity models were tested for their ability to produce unbiased clear-sky radiances when forced with buoy-observed surface winds (within 30 minutes of a GPM overpass) and MERRA atmospheric profiles: FASTEM4/5 (as implemented in CRTM;

Liu et al. (2011)) and the Meissner and Wentz (2012) (hereafter MW) model.[1] Wind direction was not considered in this study as only the MW model is capable of representing wind direction-induced emissivity changes. Instead we include the wind-direction induced error in total model error which is derived from buoy matchups. The source of wind observations in this study is the International Comprehensive Ocean-Atmosphere Data Set version 2.5 (ICOADS; Woodruff et al. (2011); NCDC/NESDIS/NOAA (2011, updated monthly)) from April 2014-March 2015. Only observations from platforms with a known anemometer height (h_b) were considered, and all winds were adjusted to 10m assuming neutral buoyancy using the relationship (Hsu et al. 1994):

$$w_{10} = w_b(10/h_b)^{0.11}. \tag{2}$$

Before the emissivity models can be intercompared, sensor calibration must be considered. Following Meissner and Wentz (2012), a calm-wind offset (δ_0) was determined for each emissivity model and each GMI channel. These offsets were obtained by first selecting a subset of ICOADS observations with 10m winds less than 3.5 m s^{-1}, where the emissivity-wind relationship is linear. To filter out clouds, observations were excluded if the polarization difference at 89 GHz was less than an SST-dependent threshold representing a cloud liquid water path of 0.01 kg m^{-2} under average atmospheric conditions or the spatial standard deviation (within 15 km) of 89 GHz Tb was greater than 2 K. The RTM was then forced with the observed SST and wind speed and interpolated MERRA atmospheric profile. The offsets were then calculated in order to minimize the bias between observed and simulated GMI brightness temperatures. No offsets were applied to the 183 GHz channels, as these were not sensitive to the surface emissivity in the matchups. The offsets and root-mean-square error (after offsets have been applied) are given for each channel and emissivity model in Table 1. The biases are different for each model at low frequencies, but similar or identical at 166 GHz, indicating low sensitivity of the brightness temperatures to emis-

[1]Note that the MW model does not include frequencies higher than 90 GHz and FASTEM5 was substituted at these frequencies.

sivity at these channels and therefore low confidence in the offsets, which are likely influenced by the water vapor absorption model and/or absolute calibration of GMI. The root-mean-square-error (rmse) values, which are not sensitive to the choice of emissivity model, represent the error from other components of the forward model (such as wind direction and water vapor absorption) plus instrument noise, and are used as the diagonal components of $\mathbf{S_y}$.

Next, each emissivity model was evaluated under the full range of conditions encountered in the GMI buoy overpasses. The retrieval was performed with each emissivity model and the retrieved winds are compared with observations in Figure 2. These results were filtered to remove precipitation by applying a maximum threshold of 1.0 for the normalized cost function. It is apparent from these results that the MERRA analysis is biased high at observed wind speeds below 3 m s^{-1} and biased low above this threshold. The retrievals using the different emissivity models behave similarly to each other up to about 8 m s^{-1} and remove most of this bias, but diverge due to different foam models (implicit in MW and explicit in FASTEM 4/5). At observed wind speeds greater than 15 m s^{-1}, FASTEM4 begins to diverge below the observed wind speed whereas FASTEM5 diverges above more severely. The MW model gives a slight low bias of as much as 1 m s^{-1} at 10-15 m s^{-1} but recovers to near zero at higher speeds. The overall root-mean-squared error in clear conditions for the MW model is 1.3 m s^{-1} (equivalent to WindSat) and, because of its low bias over the range of observed wind speeds, is chosen to generate the DPR GMFs.

The DPR GMF was generated by averaging the observed σ_0 from the DPR Level 2 product (Iguchi and Meneghini 2014), removing the two-way attenuation from gases and cloud liquid water (which are determined from the GMI retrievals), in wind speed bins with 0.5 m s^{-1} spacing from 0 to 10 m s $^{-1}$, 1 m s^{-1} spacing between 10 and 20 m s^{-1}, and 2 m s^{-1} spacing above 20 m s^{-1}. Note that all of the results presented in this manuscript are from observations taken between 25 August 2014 (when the most recent phase shift code for DPR was implemented) and 30 April

2015. Earlier observations used different phase shift codes and attenuator settings, which had some slight impact on the GMFs (not shown). The standard deviation in each bin is also calculated as is the correlation coefficient in the case of the matched KuPR-KaPR beams. The standard deviation serves as an implicit indicator of the quality of the derived GMF: Low values are desirable because they indicate that the 10m wind speed retrieved by GMI is sufficient to represent the sea state for the purposes of reproducing σ_0, and, when used in the combined framework, provide a stronger constraint on the PIA contributed by the precipitation column. The theoretical minimum standard deviation of σ_0 for DPR, assuming the signal-to-noise ratio is large (true under almost all non-rain conditions), depends on the number of independent samples, N, taken. If the surface is modeled as a Rayleigh target (an incoherent sum from many specular points on the surface without any dominant scattering contribution) and a logarithmic receiver is used, then the standard deviation in dB is given by (Sauvageot 1992):

$$std(\sigma_0) = \frac{5.57}{\sqrt{N}}, \tag{3}$$

where N depends on incidence angle and varies between 100 and about 110 . Using these numbers, the nominal standard deviation in σ_0, from sampling alone, is a bit more than 0.5 dB.[2] Values higher than 0.5 dB could be caused by random errors in the GMI wind reference (this is compounded when the sensitivity of σ_0 to wind is high) or that something other than wind speed is contributing the variation of σ_0, resulting in diminished impact of the σ_0 observation on the precipitation retrieval. In Figure 3, the standard deviation of σ_0 for the KuPR, in normal scan (NS) mode, and KaPR, in matched-scan (MS) and high-sensitivity (HS) modes, is shown as a function of DPR incidence angle for three wind speed bins centered on 0.5 m s^{-1}, 5 m s^{-1}, and 15 m s^{-1}.

[2]For off-nadir incidence, where there are multiple samples from the surface, a case can be made for integrating over all the data from the surface. This should reduce the standard deviation of the σ_0; however, in the DPR processing, the σ_0 is based on the peak return power, not the integrated power.

At the low wind speed, the standard deviation is quite high (nearly 10 dB), particularly off nadir, but smaller (still 2-4 dB) near nadir at both frequencies (the lower Ku values are likely due to the saturation of the KuPR receiver). As the wind becomes calm, the surface is nearly specular and the sensitivity to small changes in wind speed is quite high off nadir, so random error in the reference wind is thought to primarily contribute to the large standard deviation there. Long-period swell also provides an increasing contribution to variation in σ_0 (Tran et al. 2007) that is unrelated to the local wind speed. Finally, since the change in σ_0 with respect to incidence angle is also high at low wind speeds, small changes in the incidence angle (the standard deviation of DPR incidence angle was around 0.01° in each angle bin) may also contribute to the high standard deviation at off-nadir angles.

At moderate and high wind speeds, the standard deviations are much lower and the pattern is shifted slightly to relatively high values near nadir and at the largest off-nadir angles, with minima around 9° for KuPR. Specular effects can again explain the near-nadir maximum, whereas the off-nadir maxima are likely a result of wind direction sensitivity (Wentz et al. 1984). The KaPR standard deviations are slightly higher for the MS than the HS data due to the shorter pulse width, and are qualitatively similar to the KuPR data. The effect of more stringent quality control (reduction of the cloud LWP, its spatial variability, and cost function thresholds by 50%; denoted QC2 in Figure 3) is also most evident here in reducing the KaPR standard deviation, but the differences are negligible enough (0.01 dB) that the original thresholds (QC1) are used to generate databases for the combined algorithm as this choice of thresholds provides more data, especially at higher wind speeds.

The two-dimensional GMFs of σ_0 are shown in Figure 4. Most of the variability is exhibited at low wind speeds at both Ku and Ka bands[3]. However, σ_0 continues to decrease near nadir for wind speeds as high as 30 m s^{-1}, which is approximately the upper limit of the reliable data that has been collected so far. Off-nadir, σ_0 appears to reach maxima at increasing wind speeds with incidence angle. The standard deviation of σ_0 reaches minima near the 0.5 dB sampling limit at 5-15° and wind speeds between 5 and 10 m s^{-1}. There is also a minimum in the standard deviation at Ku band (but not Ka band) at very low wind speeds near nadir. This is an artifact of the saturation of the Ku receiver when $\sigma_0 \geq 22.5$ dB (The Ka receiver saturates closer to 40 dB, which is only observed over some land and ice surfaces). The higher standard deviations at the off-nadir angles are likely a result of wind-direction induced variability in σ_0. In Figure 4f the observed Ku-band σ_0 is compared to the cutoff-invariant two-scale model (Soriano and Guérin 2008) using the Durden-Vesecky single-amplitude wave spectra (Durden and Vesecky 1985). This model appears to produce a flatter σ_0 when viewed with respect to incidence angle at low wind speeds, but at winds above about 8 m s^{-1} has a comparable shape to the observed GMF minus a small (1 dB) offset. These results are consistent with the comparisons of this model to airborne observations of σ_0 reported by Majurec et al. (2014).

The Ku-Ka σ_0 correlation (Figure 4e) is an important component of the dual-frequency surface reference technique (DSRT; Meneghini et al. (2012)). In the DSRT, σ_0 is replaced by the differential σ_0:

$$\delta\sigma_0 = \sigma_0(Ka) - \sigma_0(Ku) \tag{4}$$

and the method provides an estimate of the differential PIA, A(Ka)-A(Ku). The errors in both single-frequency SRT and DSRT methods are dominated by the fluctuations in the rain-free ref-

[3] the Ka HS GMF is not shown, but is essentially identical to the MS data with a -0.2 dB offset owing to the inability of the larger pulse width to capture the surface peak as effectively, especially near nadir.

erence data: σ_0 and $\delta\sigma_0$. As the correlation between σ_0(Ku) and σ_0(Ka) increases, the variance in $\delta\sigma_0$ decreases so that the DSRT provides a potentially more accurate estimate of the path attenuations. The correlations, which are near 0.8 in most DPR angle bins when all wind speeds are considered, reduce to 0.1-0.4 for most wind speeds > 5 m s^{-1} and off-nadir incidence angles. This suggests that wind is responsible for most of the covariance in Ku and Ka σ_0 but near-nadir and at low winds the stronger correlations make the DSRT technique particularly useful.

3. Combined Radar-Radiometer Retrieval of Precipitation and Surface Wind

The MW emissivity model (optimized for GMI) and DPR wind-σ_0 GMFs described in section 2 are implemented in the forward modeling component of the GPM Combined Radar Radiometer (CORRA) retrieval algorithm. A description of the radar component of this algorithm is given by Grecu et al. (2011) and a more complete description of the algorithm architecture can be found in the Algorithm Theoretical Basis Document (Olson and Masunaga 2015); for the purposes of this manuscript, a brief summary and example case are presented in this section followed by validation statistics. It is difficult to directly ascertain the improvement (if any) in rainfall estimates over ocean owing to the lack of reliable direct measurements, but the algorithm can be assessed as to how well the forward model matches GPM observations and buoy observations of wind speed. The impact on retrieved precipitation amounts is also shown in this section.

a. Algorithm Description

The CORRA algorithm uses an ensemble filter technique (Evensen 2006) to retrieve a set of precipitation profiles that are consistent with observations from KuPR, GMI, and KaPR (where available). The first step in this process is the creation of an ensemble of solutions that fit the observed KuPR reflectivity profile without any consideration of the GMI, KaPR, or KuPR σ_0 observations.

The randomly perturbed properties of each profile solution include the vertical profile of the hydrometer particle size distribution (PSD) intercept parameter (N_w), degree of non-uniform beam filling ,the cloud liquid water profile, relative humidity, and 10m wind speed. For each solution, the associated Ku and Ka σ_0, Ka reflectivities, and GMI radiances are calculated. The calculation of Ka reflectivity's accounts for multiple scattering enhancements using the multiscatter library developed by Hogan and Battaglia (2008).

The ensemble is then filtered using the observed Ku σ_0, GMI radiances, and Ka reflectivities and σ_0 (where available). This is done by constructing an $n_{var} \times n_{memb}$ vector $\mathbf{X_{ens}}$ representing the ensemble variables to be updated, including the perturbed variables, e.g., N_w and 10m wind, and derived/forward modeled variables, e.g., precipitation rate and brightness temperature. A separate $n_{obs} \times n_{memb}$ vector $\mathbf{Y_{ens}}$ consists of the forward modeled variables corresponding to the $n_{obs} \times 1$ observation vector $\mathbf{Y_{obs}}$ ($\mathbf{R}$ is the corresponding observation error), which contains the observed σ_0, brightness temperatures, and Ka reflectivities. The ensemble state vector $\mathbf{X_{ens}}$ is then updated using the sample covariance:

$$\mathbf{X_{ens}} = \mathbf{X_{ens}} + \mathbf{Cov_{XY}}(\mathbf{Cov_{YY}} + \mathbf{R})^{-1}(\mathbf{Y_{obs}} - \mathbf{Y_{ens}}). \tag{5}$$

The algorithm output is derived from the updated ensemble and includes both mean and standard deviations of the geophysical parameters of the ensemble and forward modeled observations. This update is done separately for the Ku-only full swath (denoted as NS in GPM products) and Ku+Ka inner swath (MS products).

b. Example Case

To illustrate the update process described by Eq. 5, the retrieval algorithm is applied to a GPM overpass of a developing cyclone off the eastern coast of the United State on 26 January 2015 (Figure 5). This case provides an opportunity to examine the algorithm under a variety of precipitation and surface wind conditions.

The correlations (calculated from the initial, unfiltered ensemble) between the each observation type and the surface rain rate, as well as the correlations between each observation type and the 10m wind speed, are shown in Figure 6 for both radar frequencies and the horizontally-polarized GMI channels from 10-36 GHz (which are most sensitive to rain and wind over water surfaces). It is evident from these sensitivities that algorithm adjustments to precipitation rate in convective rain (echoes greater than 40 dBZ; purple colors in Figure 5) are mostly a response to the initial Ku and Ka σ_0 error, whereas adjustments in stratiform rain are mostly a response to the Ka σ_0 and GMI Tbs (note that in the heaviest rain, the correlation between rain rate and 36H Tb becomes negative as scattering dominates over emission). Note that in extremely heavy precipitation with large amounts of ice aloft, the variability of Ka σ_0 due to multiple scattering begins to overwhelm the attenuation, and the correlation decreases. In these cases, the algorithm relies mostly on Ku σ_0 to adjust the initial ensemble rain rates. In light and moderate rainfall, the 10m wind adjustment is mostly a response to Ku σ_0, especially away from the approximately 9° incidence angle at which Ku σ_0 is insensitive to wind. Nevertheless there is some sensitivity of the 10 and 19 GHz radiances and Ka σ_0 to wind under lighter precipitation. Due to the finite number of ensemble members, there are some spurious negative correlations between wind and the Tbs in heavier rain, but these are weak and do not substantially impact the output. The degree to which the ensemble spread is reduced after the filtering step is indicative of the overall information content in the observations for each variable of interest, and is provided as part of the standard CORRA output.

c. Internal Validation

Output from 400 GPM orbits between September 2014 and January 2015 are analyzed to assess the internal consistency between the forward model and observations before and after filtering. The mean bias and root-mean-square (rms) error between the initial ensemble mean and filtered ensemble mean for both NS (Ku+GMI) and MS (Ku+Ka+GMI) are given in Table 2. There is a general cold bias to the initial simulated brightness temperatures (Tbs) at all frequencies (although a warm bias is present in the 18 and 36 GHz channels at rain rates exceeding 10 mm hr^{-1}). Both the rms error and magnitude of the bias are reduced after filtering as expected. The MS error and bias are larger than the NS error and bias because the initial ensemble profiles are constrained by the additional Ka band information and are less free to be adjusted to match the GMI radiances. In other words, the NS retrievals are over-fit to the Tbs, which suggests an increase in their error values in **R** is warranted.

The initial and filtered rms error and bias of σ_0 is shown as a function of scan angle in Figure 7. There is a significant reduction in Ku rms error at all scan angles. The Ka error values are higher due to the stronger attenuation and multiple scattering effects, but errors are still reduced by nearly 50% after the filtering step. The bias plots show a pattern of initial errors that are consistent with a low bias in the ENV wind (too high near nadir and too low off nadir). This bias appears to be more significant than any systematic bias in the precipitation attenuation, which would have the same sign regardless of scan angle.

d. External Validation

During September 2014-January 2015, 606 buoy observations from the ICOADS database were identified as being within 30 minutes of a GPM overpass and in the KuPR swath (308 of these were within the KaPR swath) at the same time that DPR detected precipitation in the pixel nearest to the buoy location. These observations were used to validate the CORRA wind retrieval.

The wind rmse and bias are shown in Figure 8. Similar to the MERRA data analyzed in section 2, these background winds are biased high below 3 m s^{-1} and biased low at higher wind speeds relative to the buoy observations. Root-mean-square errors increase from 2 m s^{-1} to 4 m s^{-1} and NS errors are slightly higher than the MS or ENV errors. However, the bias is significantly reduced in the filtered datasets relative to the initial winds, indicating that while the retrievals are noisy, adjustments tend to be in the correct direction (this is consistent with the initial and filtered Tb and σ_0 biases as well).

The wind error is shown as a function of incidence angle in Figure 9. It is evident that the largest errors occur near the 9° incidence angle where there is little sensitivity of σ_0 to wind speed (Figures 4 and 6 illustrate this behavior). Near nadir and beyond 12° incidence angles, the sensitivity is stronger and the wind errors are much smaller. The NS errors are similar and the MS errors are smaller than the 4.26 m/s error of ASCAT under raining conditions (Portabella et al. 2012) and 3.5 m/s error Quickscat retrievals using a neural network to compensate for rain effects (Stiles and Dunbar 2010). These are also within the range of 2 to 5 m/s accuracy (depending on rain rate) of a globally-applicable rainy-atmosphere WindSat wind retrieval algorithm (Meissner and Wentz 2009). When stratified by rainfall rate, wind speed errors are similar for light (<1 mm hr^{-1}) and moderate (1 mm $hr^{-1} < R < 10$ mm hr^{-1}) precipitation rates, but increase at heavier precipitation rates as the wind-induced variability in σ_0 and brightness temperatures is overwhelmed by the precipitation effects.

e. Impact on Precipitation Retrieval

Although the retrieval of wind in precipitation is useful for many applications, one of the main purposes of this work is to improve the precipitation retrieval by enforcing an internal consistency between the surface emissivity (which depends on wind) and observed σ_0 which depends on both wind and precipitation-induced path-integrated attenuation (PIA). In this section we show the impact of switching from the SRT PIA (which infers PIA by comparing the observed σ_0 to a reference outside the precipitation) to the coupled σ_0-emissivity model.

Theoretically, the use of σ_0 as an observation (instead of SRT-derived PIA) should impact the agreement between observed and modeled Tbs in two ways: First, through adjustments to the rain column to match the observed σ_0 by changing the PIA, and second, via changes in the surface emissivity. The relative importance of these mechanisms depends on the relative sensitivity of the Tbs and σ_0 to changes in the rain column and surface wind. Figure 10 shows the change in near-surface precipitation rate retrieved by the GPM combined algorithm over ocean surfaces equatorward of 55° latitude (to eliminate possible sea ice) when the SRT PIA (single frequency for NS retrievals in top panels; DSRT in the MS retrieval shown in the bottom panels) is replaced with the observed σ_0 in the observation vector. Light precipitation (< 1 mm hr^{-1}) is increased slightly in the NS swath, predominantly at wind speeds > 10 m s^{-1} and at incidence angles less than 12°. The discontinuities in the 10-12° range are an artifact of the unavailability of the low-frequency GMI channels near the edge of the DPR swath (the deconvolution procedure requires coverage of the full footprint within the DPR swath). This suggests that GMI Tbs are driving the increase in precipitation, which is consistent with the weak Ku σ_0-precipitation correlation in light rain (Figure 6). Near the edges of the DPR swath, where the GMI Tbs are not used, there is not enough information to significantly adjust the precipitation rate because the Ku-band PIA is small relative to the uncertainty in σ_0, so the SRT and coupled method have the same information content.

At moderate (1 mm hr^{-1} < R < 10 mm hr $^{-1}$) precipitation rates, the wind-σ_0 correlation is still larger than the rain correlation at Ku band whereas Tbs are more sensitive to the precipitation (although there is still some wind sensitivity especially at 10H). This results in some compensating behavior, where it is “easier” for the algorithm to increase the wind speed to satisfy the Ku σ_0 observation but must reduce the precipitation rate to be consistent with the Tbs. In heavy rain (> 10 mm hr^{-1}), the ensemble variance in σ_0 and the Tbs is dominated by variance in the rain column, rather than surface wind, and where both observations are available only a very small reduction in precipitation is noted with the coupled forward model relative to the SRT method. When only Ku σ_0 is available in the outer swath, however, there is a reduction in precipitation relative to the SRT version. The mean precipitation rate from the coupled model is more consistent across the different scan angles than the SRT version (not shown) which suggests that the SRT PIA may be biased high at the off-nadir angles and wind speeds from 5-10 m s^{-1}.

The Ku-Ka (MS) retrievals are generally more stable when comparing the SRT and coupled versions of the algorithm, but some changes are still notable. The increase in light precipitation is still present, but moderate and heavy precipitation show some different behavior from the NS retrievals with increases in light winds (below about 5 m s^{-1}) and little change at higher wind speeds. There is not much sensitivity of Tb to wind at low wind speeds, so this appears to be driven by an increase in the inferred PIA in the coupled model relative to the dual-frequency SRT.

4. Summary

The Global Precipitation Measurement core satellite launched in February, 2014 carries a passive microwave imager (GMI) and dual-frequency radar (DPR) designed specifically to provide the most accurate instantaneous precipitation estimates currently available from space and serve as a reference for precipitation retrievals from other passive microwave imagers with similar channel sets (Kummerow et al. 2015). The GPM combined algorithm plays a key role in this process by providing precipitation estimates that are consistent with both GMI and DPR measurements. This algorithm uses physically-based forward models to simulate GMI and DPR measurements and it is desirable that those models use the same geophysical input parameters wherever possible.

This study explored the feasibility of using internally consistent relationships between wind, emissivity, and backscatter for water surfaces in the combined algorithm. We first evaluated the FASTEM 4/5 (Liu et al. 2011) and Meissner and Wentz (2012) emissivity models in a GMI-only non-precipitation retrieval against buoy observations obtained from the ICOADS dataset. The Meissner-Wentz model provided the lowest root-mean-square error (1.3 m s^{-1}) and was used to create a geophysical model function (GMF) for DPR Ku and Ka σ_0 as a function of 10m wind speed and incidence angle by matching the GMI retrievals to DPR observations under clear conditions.

The Meissner-Wentz emissivity model and DPR GMFs were then implemented in the GPM combined algorithm. This coupled forward model indicated that the sensitivity of σ_0 to wind at Ku band dominates the precipitation sensitivity particularly in light to moderate rain and at low wind speeds, where the brightness temperatures are more sensitive to precipitation (although there is still some wind sensitivity, particularly at 10 and 18 GHz at horizontal polarization in light and shallow precipitation). Therefore, the surface reference (SRT) estimate of the DPR path-integrated attenuation (PIA) was replaced with σ_0 in the observation vector. This is desirable because σ_0 is directly observed by DPR while the SRT PIA includes implicit assumptions and can be unphysically negative in light rain. Because σ_0 depends on both the 10m wind speed and attenuation from atmospheric gases, clouds, and precipitation, the 10m wind speed was added to the retrieval state vector.

The combined wind/precipitation retrievals were then evaluated against the ICOADS buoy dataset under precipitating conditions, which have been a challenge for surface wind retrievals from standalone passive radiometers (e.g., WindSat) or scatterometers. Although the retrievals were noisier than under clear conditions (rmse of 3.7 m s^{-1} for Ku+GMI and 3.2 m s^{-1} for Ku+Ka+GMI), there was a significant reduction in the bias from the background data provided by GANAL (-10%) to the Ku+GMI (-3%) and Ku+Ka+GMI (-5%) retrievals. The impact on precipitation retrievals was also evaluated. Ku+GMI retrievals of precipitation increased slightly on the light end ($<$ 1 mm hr^{-1}) and decreased in moderate to heavy precipitation ($>$ 1mm hr^{-1}) due to compensating effects of wind on σ_0 and emissivity requiring changes in the precipitation column to maintain consistency with the observations. The Ku+Ka+GMI retrievals, being additionally constrained by the Ka reflectivity, did not change as much although a slight increase in moderate and heavy precipitation at low wind speeds was noted.

While GPM was not designed specifically to measure ocean surface winds, this study demonstrates that such measurements are quite feasible in clear-sky conditions. In precipitation, using a coupled emissivity-backscatter GMF produces reasonable results that achieve the goal of internal consistency in the combined algorithm. The results presented here should only be considered as a proof of concept, as additional details that we did not consider, such as wind direction, the effect of rain on the scattering properties of water surfaces, and spatial correlation of the wind field, are left to future work.

Acknowledgments. This work was supported under NASA Cooperative Agreement NNX12AD03A and Precipitation Measurement Missions Program Scientist Dr. Ramesh

Kakar. We would also like to thank Dr. Thomas Meissner of Remote Sensing Systems for providing the computational codes for the Meissner-Wentz emissivity model, and Dr. Simone Tanelli of NASA JPL/CalTech for providing the cutoff-invariant two-scale Durden-Vesecky model data. Finally, we would like to thank the three anonymous reviewers whose comments and suggestions greatly improved the quality of this manuscript.

References

Albrecht, B. A., C. W. Fairall, D. W. Thomson, A. B. White, J. B. Snider, and W. H. Schubert, 1990: Surface-based remote sensing of the observed and the adiabatic liquid water content of stratocumulus clouds. *Geophysical Research Letters*, **17 (1)**, 89–92, doi:10.1029/GL017i001p00089, URL http://dx.doi.org/10.1029/GL017i001p00089.

Battaglia, A., and C. Simmer, 2008: How does multiple scattering affect the spaceborne W-Band radar measurements at ranges close to and crossing the sea-surface range? *Geoscience and Remote Sensing, IEEE Transactions on*, **46 (6)**, 1644–1651, doi:10.1109/TGRS.2008.916085.

Boukabara, S.-A., and Coauthors, 2011: MiRS: An All-Weather 1DVAR satellite data assimilation and retrieval system. *Geoscience and Remote Sensing, IEEE Transactions on*, **49 (9)**, 3249–3272, doi:10.1109/TGRS.2011.2158438.

Donnelly, W. J., J. R. Carswell, R. E. McIntosh, P. S. Chang, J. Wilkerson, F. Marks, and P. G. Black, 1999: Revised ocean backscatter models at C and Ku band under high-wind conditions. *Journal of Geophysical Research: Oceans*, **104 (C5)**, 11 485–11 497, doi:10.1029/1998JC900030, URL http://dx.doi.org/10.1029/1998JC900030.

Draper, D., D. Newell, F. Wentz, S. Krimchansky, and G. Skofronick-Jackson, 2015: The global precipitation measurement (GPM) microwave imager (GMI): Instrument overview and early onorbit performance. *IEEE Journal of Selected Topics in Applied Earth Observations and Remote Sensing*, in review.

Durden, S., and J. Vesecky, 1985: A physical radar cross-section model for a wind-driven sea with swell. *Oceanic Engineering, IEEE Journal of*, **10 (4)**, 445–451, doi:10.1109/JOE.1985.1145133.

Elsaesser, G. S., and C. D. Kummerow, 2008: Toward a fully parametric retrieval of the nonraining parameters over the global oceans. *J. Appl. Meteor. Climatol.*, **47**, 1599–1618.

Evensen, G., 2006: *Data Assimilation: The Ensemble Kalman Filter*. Springer, 280 pp.

Fernandez, D. E., J. R. Carswell, S. Frasier, P. S. Chang, P. G. Black, and F. D. Marks, 2006: Dual-polarized C- and Ku-band ocean backscatter response to hurricane-force winds. *Journal of Geophysical Research: Oceans*, **111 (C8)**, n/a–n/a, doi:10.1029/2005JC003048, URL http://dx.doi.org/10.1029/2005JC003048.

Freilich, M. H., and B. A. Vanhoff, 2003: The relationship between winds, surface roughness, and radar backscatter at low incidence angles from TRMM Precipitation Radar measurements. *J. Atmos. Oceanic Technol.*, **20**, 549–562.

GPM Science Team, 2015: GPM Level 1C R Common Calibrated Brightness Temperatures Collocated,version 04. NASA Goddard Earth Science Data and Information Services Center (GES DISC), Greenbelt, MD, USA, URL http://disc.sci.gsfc.nasa.gov/datacollection/GPM_1CGPMGMI_R_V04.html, accessed 16 May 2015.

Grecu, M., W. S. Olson, and E. N. Anagnostou, 2004: Retrieval of precipitation profiles from multiresolution, multifrequency active and passive microwave observations. *J. Appl. Meteor.*, **43**, 562–575.

Grecu, M., L. Tian, W. S. Olson, and S. Tanelli, 2011: A robust dual-frequency radar profiling algorithm. *J. Appl. Meteor. Climatol.*, **50**, 1543–1557.

Haddad, Z. S., E. A. Smith, C. D. Kummerow, T. Iguchi, M. R. Farrar, S. L. Durden, M. Alves, and W. S. Olson, 1997: The TRMM 'Day-1' radar/radiometer combined rain-profiling algorithm. *J. Meteor. Soc. Japan*, **75**, 799–809.

Hogan, R. J., and A. Battaglia, 2008: Fast lidar and radar multiple-scattering models: Part 2: Wide-angle scattering using the time-dependent two-stream approximation. *J. Atmos. Sci.*, **65**, 3636–3651.

Hou, A. Y., and Coauthors, 2014: The Global Precipitation Measurement Mission. *Bull. Amer. Meteor. Soc.*, **95**, 701–722.

Hsu, S. A., E. A. Meindl, and D. B. Gilhousen, 1994: Determining the power-law wind-profile exponent under near-neutral stability conditions at sea. *J. Appl. Meteor.*, **33**, 757–765.

Iguchi, T., T. Kozu, J. Kwiatkowski, , R. Meneghini, J. Awaka, and K. Okamoto, 2009: Uncertainties in the rain profiling algorithm for the TRMM Precipitation Radar. *J. Meteor. Soc. Japan*, **87A**, 1–30.

Iguchi, T., T. Kozu, R. Meneghini, J. Awaka, and K. Okamoto, 2000: Rain-profiling algorithm for the TRMM Precipitation Radar. *J. Appl. Meteor.*, **39**, 2038–2052.

Iguchi, T., and R. Meneghini, 2014: GPM DPR Level 2A DPR Environment V03 (GPM 2ADPR), version 03. NASA Goddard Earth Science Data and Information Services Center (GES DISC), Greenbelt, MD, USA, URL http://disc.sci.gsfc.nasa.gov/datacollection/GPM_2ADPR_V03.html, accessed 8 April 2015.

Kummerow, C. D., D. Randel, M. Kulie, N.-Y. Wang, R. Ferraro, S. J. Munchak, and V. Petkovic, 2015: The evolution of the Goddard Profiling Algorithm to a fully parametric scheme. *J. Atmos. Oceanic Technol.*, accepted.

Li, L., E. Im, L. Connor, and P. Chang, 2004: Retrieving ocean surface wind speed from the TRMM Precipitation Radar measurements. *Geoscience and Remote Sensing, IEEE Transactions on*, **42 (6)**, 1271–1282, doi:10.1109/TGRS.2004.828924.

Li, L., E. Im, S. L. Durden, and Z. S. Haddad, 2002: A surface wind model-based method to estimate rain-induced radar path attenuation over ocean. *J. Atmos. Oceanic Technol.*, **19**, 658–672.

Liebe, H., G. Hufford, and T. Manabe, 1991: A model for the complex permittivity of water at frequencies below 1 THz. *International Journal of Infrared and Millimeter Waves*, **12 (7)**, 659–675, doi:10.1007/BF01008897, URL http://dx.doi.org/10.1007/BF01008897.

Liu, Q., F. Weng, and S. English, 2011: An improved fast microwave water emissivity model. *Geoscience and Remote Sensing, IEEE Transactions on*, **49 (4)**, 1238–1250, doi:10.1109/TGRS.2010.2064779.

Majurec, N., J. Johnson, S. Tanelli, and S. Durden, 2014: Comparison of model predictions with measurements of Ku- and Ka-band near-nadir normalized radar cross sections of the sea surface from the Genesis and Rapid Intensification Processes experiment. *Geoscience and Remote Sensing, IEEE Transactions on*, **52 (9)**, 5320–5332, doi:10.1109/TGRS.2013.2288105.

Meissner, T., and F. Wentz, 2009: Wind-vector retrievals under rain with passive satellite microwave radiometers. *Geoscience and Remote Sensing, IEEE Transactions on*, **47 (9)**, 3065–3083.

Meissner, T., and F. Wentz, 2012: The emissivity of the ocean surface between 6 and 90 GHz over a large range of wind speeds and earth incidence angles. *Geoscience and Remote Sensing, IEEE Transactions on*, **50 (8)**, 3004–3026, doi:10.1109/TGRS.2011.2179662.

Meneghini, R., T. Iguchi, T. Kozu, L. Liao, K. Okamoto, J. A. Jones, and J. Kwiatkowski, 2000: Use of the surface reference technique for path attenuation estimates from the TRMM Precipitation Radar. *J. Appl. Meteor.*, **39**, 2053–2070.

Meneghini, R., J. A. Jones, T. Iguchi, K. Okamoto, and J. Kwiatkowski, 2004: A hybrid surface reference technique and its application to the TRMM Precipitation Radar. *J. Atmos. Oceanic Technol.*, **21**, 1645–1658.

Meneghini, R., L. Liao, S. Tanelli, and S. Durden, 2012: Assessment of the performance of a dual-frequency surface reference technique over ocean. *Geoscience and Remote Sensing, IEEE Transactions on*, **50 (8)**, 2968–2977, doi:10.1109/TGRS.2011.2180727.

Migliaccio, M., and A. Reppucci, 2006: A review of sea wind vector retrievals by means of microwave remote sensing. *Proceedings of the European Microwave Association Vol*, **136**, 140.

Mitrescu, C., T. L'Ecuyer, J. Haynes, S. Miller, and J. Turk, 2010: Cloudsat precipitation profiling algorithm – model description. *J. Appl. Meteor. Climatol.*, **49**, 991–1003.

Munchak, S. J., and C. D. Kummerow, 2011: A modular optimal estimation method for combined radar-radiometer precipitation profiling. *J. Appl. Meteor. Climatol.*, **50**, 433–448.

NASA/GMAO, 2008: MERRA Reanalysis Data. NASA Goddard Earth Science Data and Information Services Center (GES DISC), Greenbelt, MD, USA, URL http://disc.sci.gsfc.nasa.gov/mdisc, accessed 27 February 2015.

NCDC/NESDIS/NOAA, 2011, updated monthly: International Comprehensive Ocean-Atmosphere Data Set Release 2.5, Individual Observations. NOAA NCDC, Asheville, NC, USA, URL http://www1.ncdc.noaa.gov/pub/data/icoads2.5/, accessed 8 May 2015.

Negri, A. J., R. F. Adler, and C. D. Kummerow, 1989: False-color display of Special Sensor Microwave/Imager (SSM/I) data. *Bull. Amer. Meteor. Soc.*, **70**, 146–151.

O'Dell, C. W., F. J. Wentz, and R. Bennartz, 2008: Cloud liquid water path from satellite-based passive microwave observations: A new climatology over the global oceans. *J. Climate*, **21**, 1721–1739.

Olson, W. S., and H. Masunaga, 2015: GPM Combined Radar - Radiometer Precipitation Algorithm Theoretical Basis Document (Version 3). NASA ATBD, NASA GSFC, 59 pp. URL http://pps.gsfc.nasa.gov/Documents/Combined_algorithm_ATBD.2014.restore16-1.pdf.

Portabella, M., A. Stoffelen, W. Lin, A. Turiel, A. Verhoef, J. Verspeek, and J. Ballabrera-Poy, 2012: Rain effects on ascat-retrieved winds: Toward an improved quality control. *Geoscience and Remote Sensing, IEEE Trans. Geosci. Rem*, **50 (7)**, 2495–2506.

Quilfen, Y., C. Prigent, B. Chapron, A. A. Mouche, and N. Houti, 2007: The potential of QuikSCAT and WindSat observations for the estimation of sea surface wind vector under severe weather conditions. *Journal of Geophysical Research: Oceans*, **112 (C9)**, n/a–n/a, doi:10.1029/2007JC004163, URL http://dx.doi.org/10.1029/2007JC004163.

Rapp, A. D., M. Lebsock, and C. Kummerow, 2009: On the consequences of resampling microwave radiometer observations for use in retrieval algorithms. *J. Appl. Meteor. Climatol.*, **48**, 1981–1993.

Rienecker, M. M., and Coauthors, 2011: MERRA: NASA's modern-era retrospective analysis for research and applications. *J. Climate*, **24**, 3624–3648.

Rosenkranz, P. W., 1998: Water vapor microwave continuum absorption: A comparison of measurements and models. *Radio Science*, **33 (4)**, 919–928, doi:10.1029/98RS01182, URL http://dx.doi.org/10.1029/98RS01182.

Sauvageot, H., 1992: *Radar meteorology*. Artech House Publishers.

Seto, S., and T. Iguchi, 2007: Rainfall-induced changes in actual surface backscattering cross sections and effects on rain-rate estimates by spaceborne precipitation radar. *J. Atmos. Oceanic Technol.*, **24**, 1693–1709.

Soriano, G., and C.-A. Guérin, 2008: A cutoff invariant two-scale model in electromagnetic scattering from sea surfaces. *Geoscience and Remote Sensing Letters, IEEE*, **5 (2)**, 199–203.

Stiles, B., and R. Dunbar, 2010: A neural network technique for improving the accuracy of scatterometer winds in rainy conditions. *Geoscience and Remote Sensing, IEEE Transactions on*, **48 (8)**, 3114–3122.

Stiles, B., and S. Yueh, 2002: Impact of rain on spaceborne Ku-band wind scatterometer data. *Geoscience and Remote Sensing, IEEE Transactions on*, **40 (9)**, 1973–1983, doi:10.1109/TGRS.2002.803846.

Tran, N., B. Chapron, and D. Vandemark, 2007: Effect of long waves on Ku-band ocean radar backscatter at low incidence angles using TRMM and altimeter data. *Geoscience and Remote Sensing Letters, IEEE*, **4 (4)**, 542–546, doi:10.1109/LGRS.2007.896329.

Tretyakov, M., V. Parshin, M. Koshelev, V. Shanin, S. Myasnikova, and A. Krupnov, 2003: Studies of 183 GHz water line: Broadening and shifting by air, N_2 and O_2 and integral intensity measurements. *Journal of Molecular Spectroscopy*, **218 (2)**, 239 – 245, doi:http://dx.doi.org/10.1016/S0022-2852(02)00084-X, URL http://www.sciencedirect.com/science/article/pii/S002228520200084X.

Uhlhorn, E. W., P. G. Black, J. L. Franklin, M. Goodberlet, J. Carswell, and A. S. Goldstein, 2007: Hurricane surface wind measurements from an operational stepped frequency microwave radiometer. *Mon. Wea. Rev.*, **135**, 3070–3085.

Weissman, D. E., B. W. Stiles, S. M. Hristova-Veleva, D. G. Long, D. K. Smith, K. A. Hilburn, and W. L. Jones, 2012: Challenges to satellite sensors of ocean winds: Addressing precipitation effects. *J. Atmos. Oceanic Technol.*, **29**, 356–374.

Wentz, F. J., S. Peteherych, and L. A. Thomas, 1984: A model function for ocean radar cross sections at 14.6 GHz. *Journal of Geophysical Research: Oceans*, **89 (C3)**, 3689–3704, doi:10.1029/JC089iC03p03689, URL http://dx.doi.org/10.1029/JC089iC03p03689.

Woodruff, S. D., and Coauthors, 2011: ICOADS Release 2.5: Extensions and enhancements to the surface marine meteorological archive. *International Journal of Climatology*, **31 (7)**, 951–967, doi:10.1002/joc.2103, URL http://dx.doi.org/10.1002/joc.2103.

Yueh, S., W. Tang, A. Fore, G. Neumann, A. Hayashi, A. Freedman, J. Chaubell, and G. Lagerloef, 2013: L-band passive and active microwave geophysical model functions of ocean surface winds and applications to Aquarius retrieval. *Geoscience and Remote Sensing, IEEE Transactions on*, **51 (9)**, 4619–4632, doi:10.1109/TGRS.2013.2266915.

LIST OF TABLES

TABLE 1. Bias (before applying offsets) and root-mean-square error (after applying offsets), in K, of clear-sky, nearly-calm wind (< 3.5 m s^{-1}) simulated brightness temperatures forced with buoy observations of SST and 10m wind and MERRA atmospheric parameters. No offsets were applied to the 183 GHz channels.

	FASTEM4		FASTEM5		Meissner-Wentz	
Channel	bias	rmse	bias	rmse	bias	rmse
10.65V	1.6	0.8	0.6	0.7	-1.0	0.7
10.65H	2.9	0.9	-0.4	0.9	-0.7	0.9
18.7V	0.6	1.0	0.2	1.0	-0.5	1.0
18.7H	2.3	1.6	0.3	1.5	0.1	1.5
23.8V	-0.5	1.5	-0.5	1.4	-0.6	1.4
36.64V	0.6	0.9	0.6	0.9	0.6	0.9
36.64H	2.9	1.6	2.1	1.6	1.3	1.5
89V	-0.4	1.0	0.0	1.0	0.8	1.1
89H	1.5	2.2	2.5	2.2	1.7	2.2
166V	-0.1	1.4	-0.3	1.4	-0.3	1.4
166H	0.1	2.8	0.2	3.1	0.3	3.2
183±3	-2.8	3.7	-2.8	3.6	-3.0	3.6
183±7	-0.7	1.8	-0.9	1.9	-1.0	1.9

TABLE 2. Root-mean-square error and bias of ensemble-mean deconvolved GPM Microwave Imager (GMI) radiances before and after filtering.

	10V	10H	18V	18H	23V	36V	36H	89V	89H
Initial rmse (K)	6.7	11.3	11.6	19.8	12.0	15.5	26.6	23.1	25.9
Initial Bias (K)	-3.7	-7.2	-6.0	-10.9	-6.5	-9.0	-14.3	-16.1	-16.0
NS rmse (K)	4.6	7.1	7.2	11.1	8.1	9.9	15.1	16.2	16.9
NS Bias (K)	-1.7	-3.6	-2.9	-5.0	-3.3	-4.8	-5.7	-11.6	-8.2
MS rmse (K)	8.1	9.8	11.1	15.1	12.7	13.6	20.0	22.0	24.8
MS Bias (K)	-2.5	-4.0	-4.4	-6.8	-5.2	-5.9	-8.4	-13.2	-12.5

LIST OF FIGURES

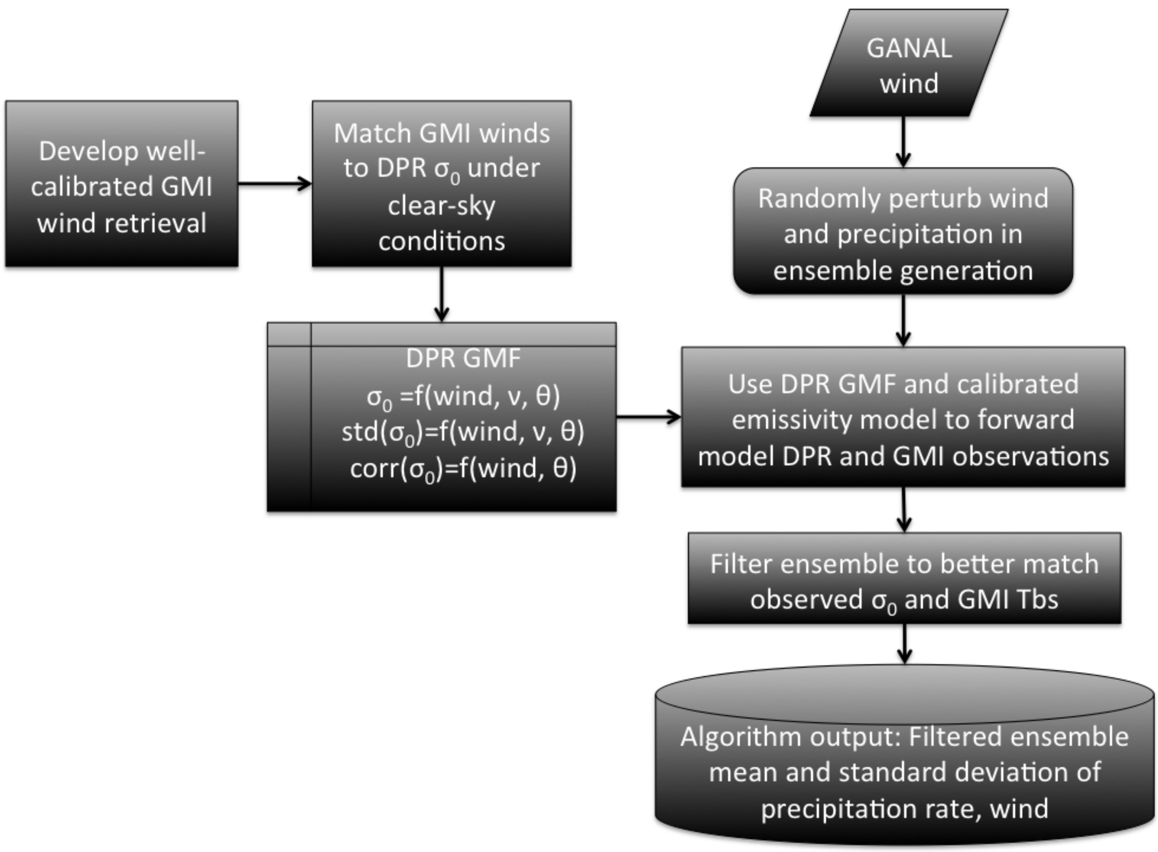

FIG. 1. Flow chart of the process by which the DPR geophysical model function (GMF) is derived and used by the combined DPR-GMI precipitation algorithm.

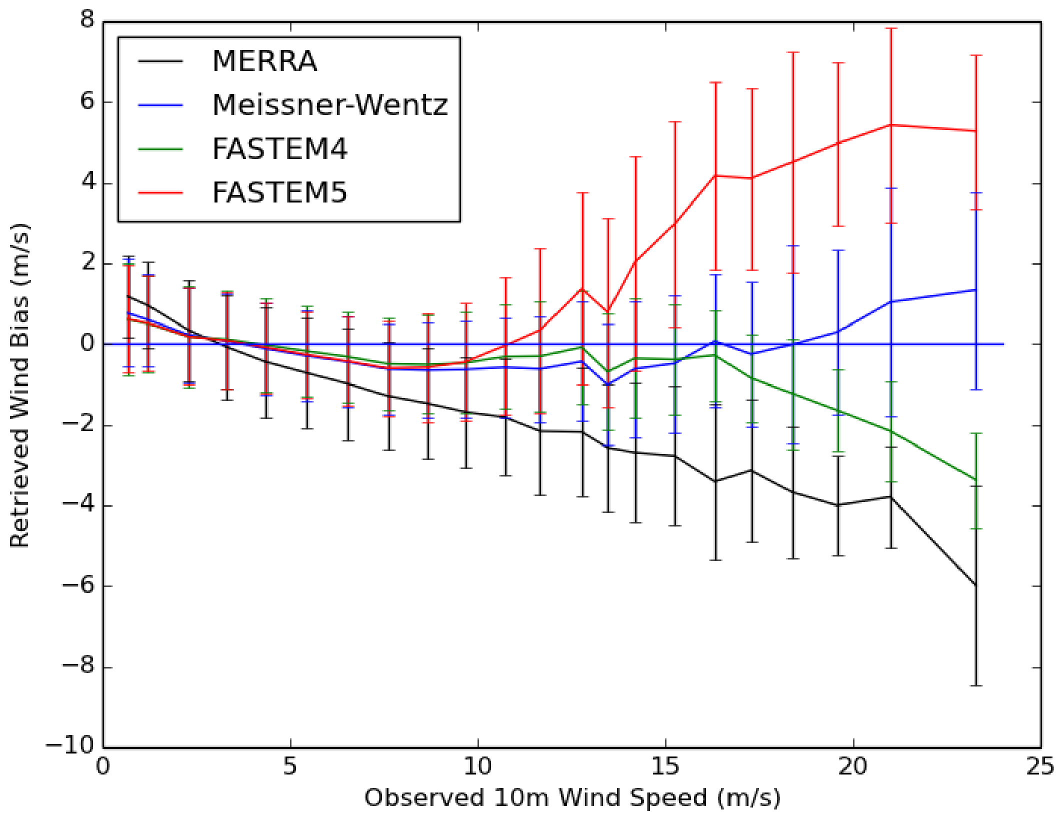

FIG. 2. MERRA and GMI-retrieved wind speed bias relative to ICOADS buoy observations from March-December 2014. Error bars represent 1 standard deviation of the difference between observed and retrieved wind speeds in each bin.

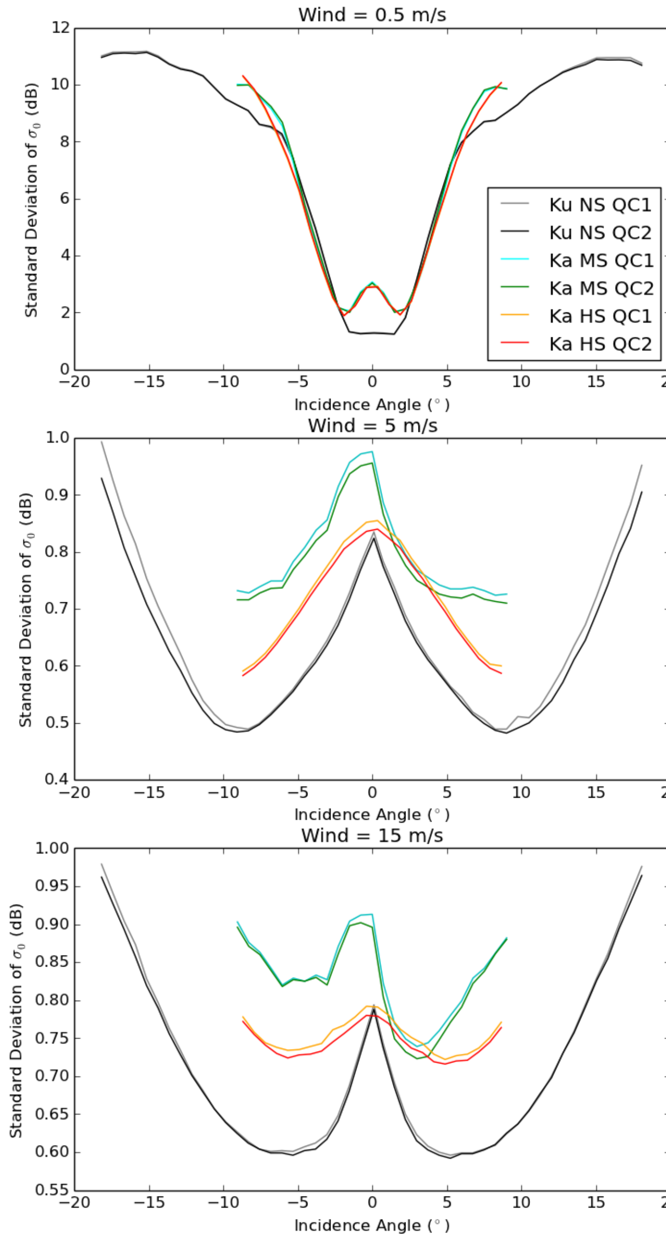

FIG. 3. Standard deviation of σ_0 in three wind speed bins: 0.5 m s^{-1} (top), 5 m s^{-1} (middle), and 15 m s^{-1} (bottom). The different colors represent different frequencies, DPR modes (NS = Normal Scan, MS = Matched Scan, HS = High Sensitivity), and quality control of the reference wind.

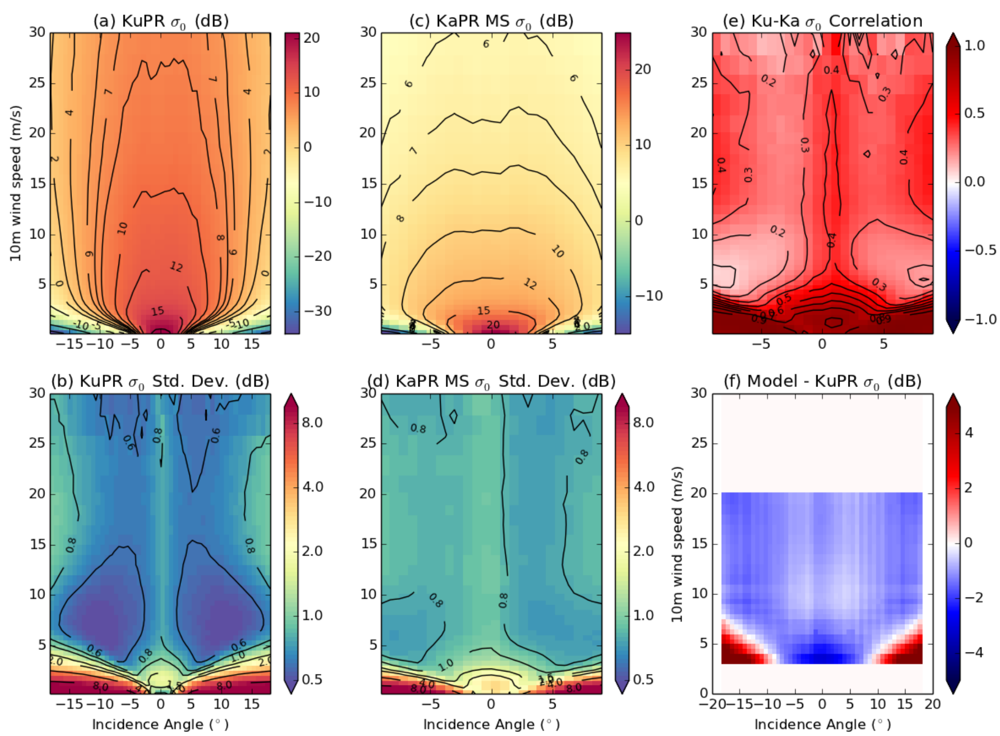

FIG. 4. The two-dimensional geophysical model functions (GMFs) of σ_0, its standard deviation, Ku-Ka correlation, and difference between the Durden-Vesecky single-amplitude model and observations at Ku band are shown as a function of 10m wind speed and incidence angle.

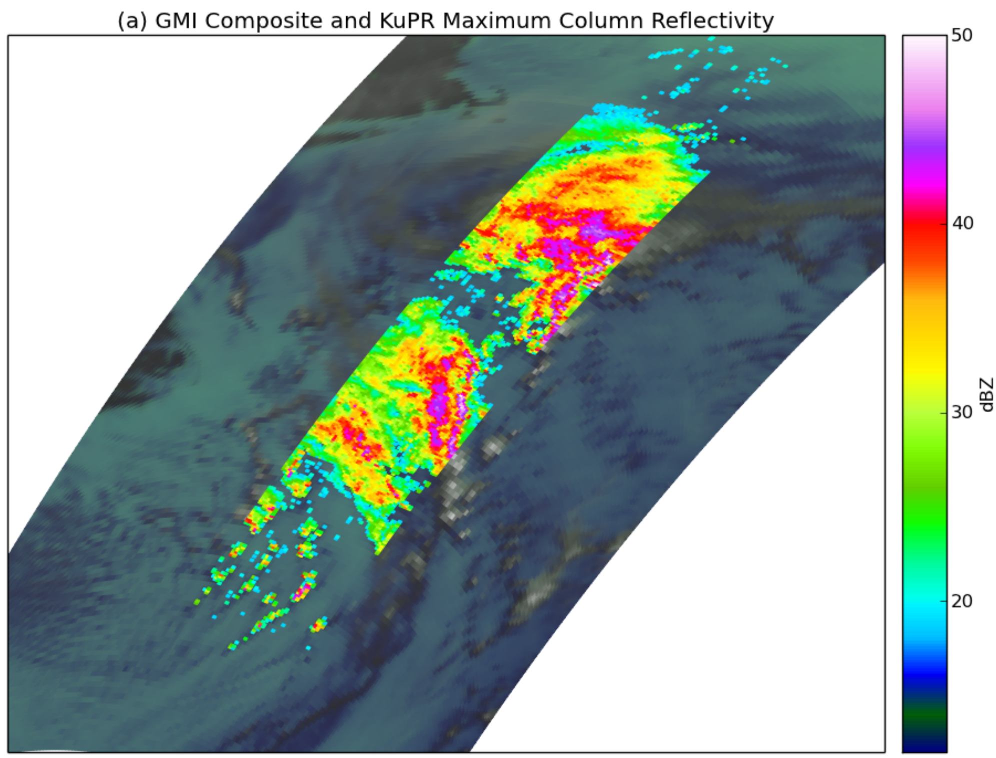

FIG. 5. False-color GMI composite and KuPR maximum column observed reflectivity at 2204 UTC 26 January 2015. The GMI composite is from the 89 GHz V and H and 36 GHz V channels following the Negri et al. (1989) scheme.

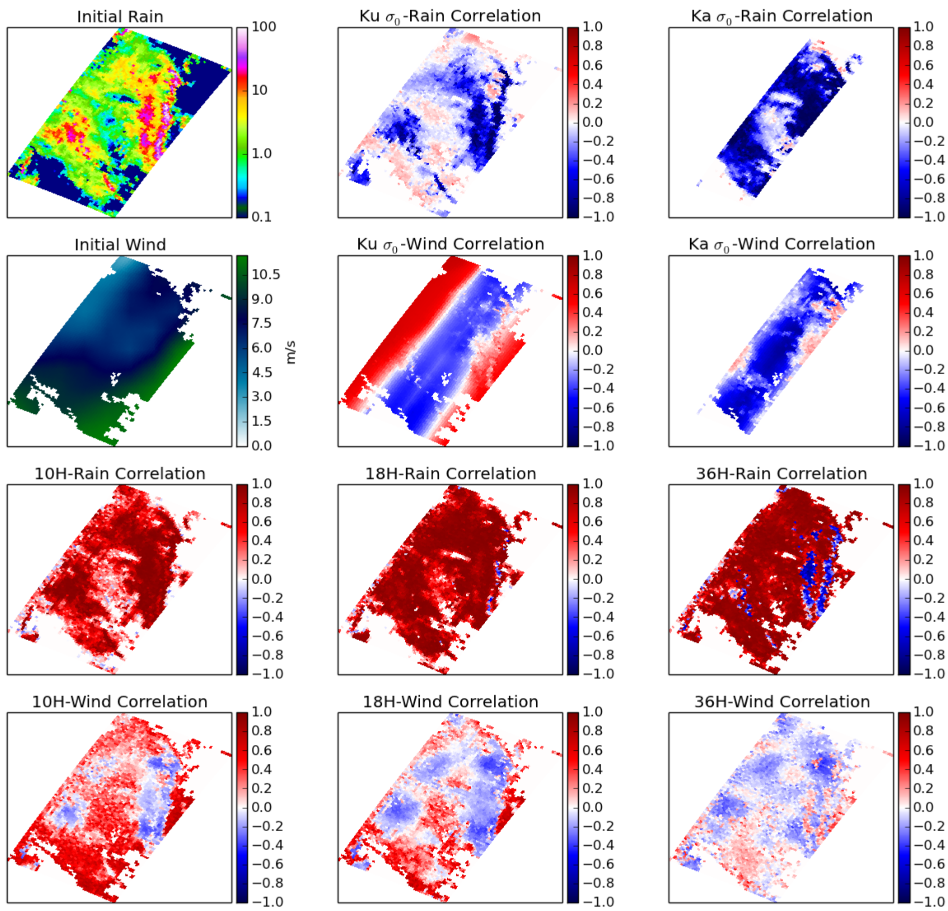

709 FIG. 6. Correlations of Ku and Ka σ_0 and 10.65, 18.7, and 36.6 GHz horizontally-polarized brightness
710 temperatures to surface rain rate and 10m wind speed, derived from the initial ensemble of solutions to each
711 radar profile.

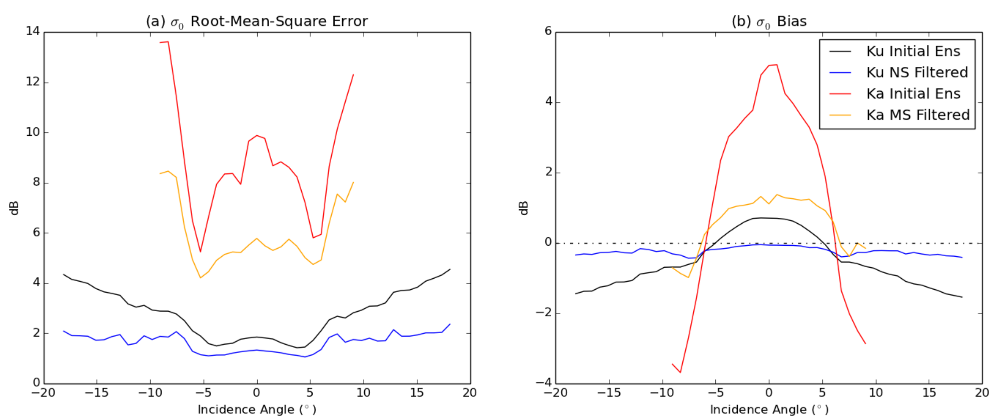

FIG. 7. Root-mean-square error (a) and bias (b) of the initial and filtered ensemble mean σ_0 as a function of incidence angle.

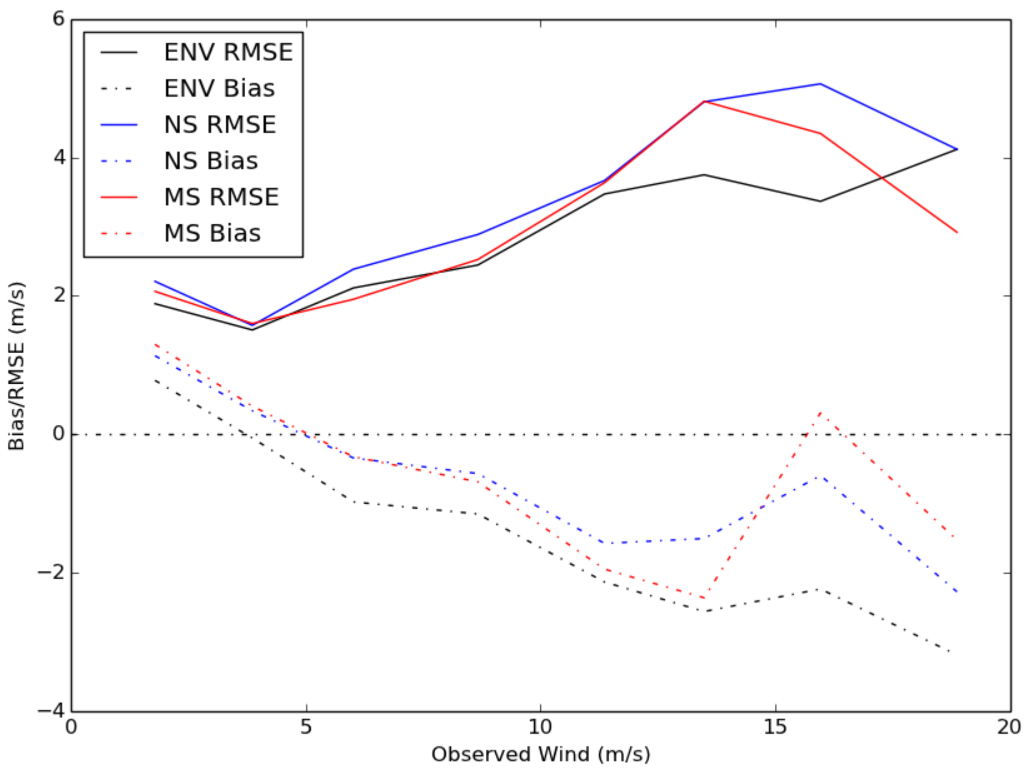

FIG. 8. Background (JMA Global Analysis GANAL; 2A-ENV) and retrieved wind root-mean-square error and bias relative to ICOADS buoy observations in precipitating pixels.

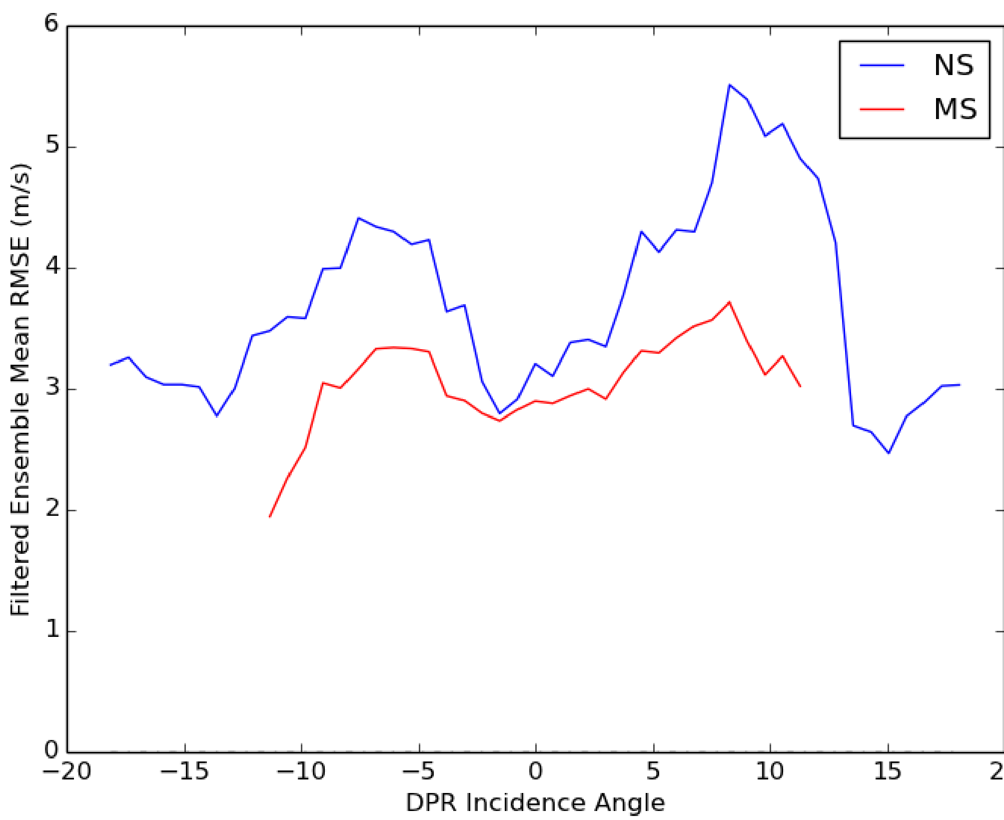

716 FIG. 9. Retrieved wind root mean square error as a function of DPR incidence angle. The data are smoothed
717 using a 7-bin centered average in order to reduce noise from the small sample size in each angle bin.

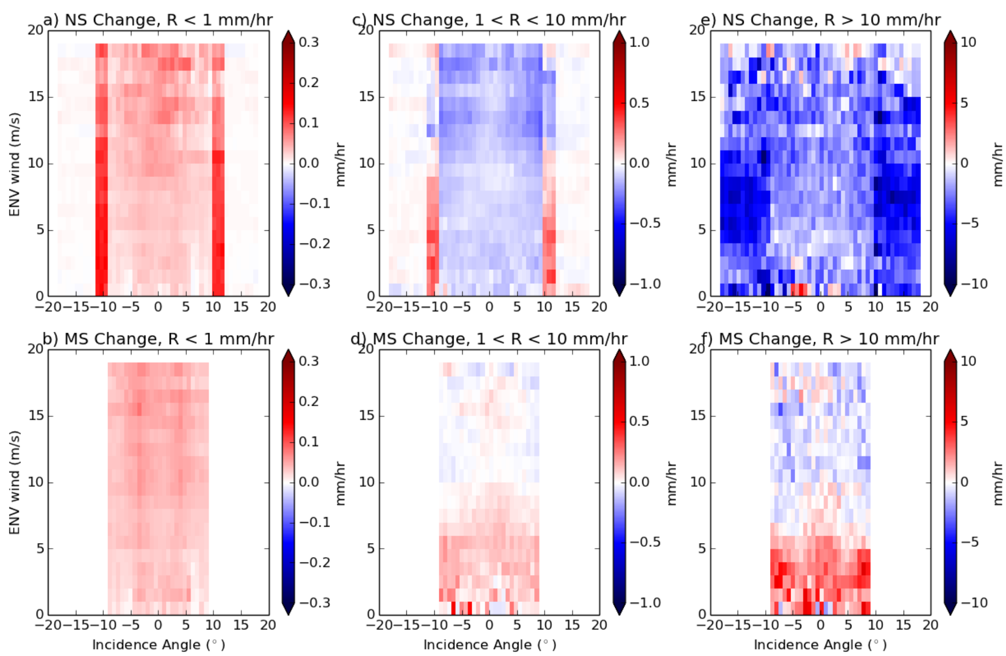

FIG. 10. Change in GPM combined algorithm precipitation, as a function of wind speed and incidence angle, when the Surface Reference Technique (SRT) path-integrated attenuation (PIA) is replaced with the observed σ_0 in the observation vector and coupled σ_0-emissivity model is used in the forward model. The ENV wind and SRT-based precipitation are used as reference values.